Nanocellulose-derived carbon/g-C3N4 heterojunction with a hybrid electron transfer pathway for highly photocatalytic hydrogen peroxide production

Yiwei Shan, Ying Guo, Yu Wang, Xiran Du, Jun Yu, Hao Luo, Hui Wu, Bruno Boury, He Xiao, Liulian Huang, et al.

▶ **To cite this version:**

Yiwei Shan, Ying Guo, Yu Wang, Xiran Du, Jun Yu, et al.. Nanocellulose-derived carbon/g-C3N4 heterojunction with a hybrid electron transfer pathway for highly photocatalytic hydrogen peroxide production. Journal of Colloid and Interface Science, 2021, 599, pp.507-518. 10.1016/j.jcis.2021.04.111 . hal-03276337

HAL Id: hal-03276337
https://hal.umontpellier.fr/hal-03276337

Submitted on 9 May 2023

HAL is a multi-disciplinary open access archive for the deposit and dissemination of scientific research documents, whether they are published or not. The documents may come from teaching and research institutions in France or abroad, or from public or private research centers.

L'archive ouverte pluridisciplinaire **HAL**, est destinée au dépôt et à la diffusion de documents scientifiques de niveau recherche, publiés ou non, émanant des établissements d'enseignement et de recherche français ou étrangers, des laboratoires publics ou privés.

Distributed under a Creative Commons Attribution - NonCommercial 4.0 International License

Version of Record: https://www.sciencedirect.com/science/article/pii/S0021979721006275
Manuscript_36f113590bac4cd3dee1f4c4bf6fbc00

Nanocellulose-derived carbon/g-C_3N_4 heterojunction with a hybrid electron transfer pathway for highly photocatalytic hydrogen peroxide production

Yiwei Shan [a], Ying Guo [a], Yu Wang [a], Xiran Du [a], Jun Yu [a], Hao Luo [a], Hui Wu [a], Bruno Boury [b,*], He Xiao [a,*], Liulian Huang [a], Lihui Chen [a]

[a] College of Material Engineering, Fujian Agriculture and Forestry University, Fuzhou, 350108, China

[b] ICGM, University of Montpellier, CNRS, ENSCM, Montpellier, France

Corresponding authors: Bruno Boury (bruno.boury@umontpellier.fr),

He Xiao (xiaohe_river@163.com)

Abstract

Using oxygen reduction for the photocatalytic production of hydrogen peroxide (H_2O_2) has been considered a green and sustainable route. In the present study, to achieve high efficiency, graphitic carbon nitride (g-C_3N_4) was obtained using thermal polymerization from a bi-component precursor and was then assembled with cellulose nanofibers. It was found that a small quantity of cellulose nanofibers that generates carbon fibers upon pyrolysis greatly improves the photocatalytic activity compared with that of g-C_3N_4 alone. The well-defined carbon/g-C_3N_4 heterojunction-type material exhibits as high as 1.10 mmol L^{-1} h^{-1} of photo-production of H_2O_2 under visible light, which is 4.2 times higher than that yielded by pristine g-C_3N_4 from a single precursor. A comprehensive characterization of the photocatalyst enables us to delineate the effect of the carbon nanofiber with respect to porosity, electron–hole separation, band gap regulation, and especially the electron transfer pathway. Our

© 2021 published by Elsevier. This manuscript is made available under the CC BY NC user license
https://creativecommons.org/licenses/by-nc/4.0/

results demonstrate that nanocellulose-derived carbon, when precisely assembled with other functional material such as a photocatalyst, is a promising promoter of their activity.

Keywords: Cellulose nanofibers; Photocatalysis; Carbon nitride; Hydrogen peroxide production; Carbon fibers

1. Introduction

Hydrogen peroxide (H_2O_2) is a promising energy storage product widely used both as an oxidant and reductant in chemical synthesis, industrial bleaching, and medical sterilization [1, 2]. Moreover, in line with the need for new answers to the increase in energy demand, H_2O_2 has been proposed as the oxidizing agent at the cathode of fuel cells with environmentally acceptable by-products, H_2O and O_2 [3]. Presently, the methods adopted to produce H_2O_2 on a large scale are anthraquinone autoxidation [4] and electrochemical synthesis [5]. These methods consume a large amount of energy and organic solvents; in addition, contamination by various organic impurities can occur and result in increased difficulties of purification [6, 7]. Consequently, new production processes must succeed in satisfying the demand for H_2O_2, resolve and eliminate the shortcomings of traditional production methods, be efficient, and above all be sustainable and environmentally friendly with respect to the principles of green chemistry.

In recent decades, photocatalysis has been employed in light-driven production of H_2O_2 through photoreduction of O_2 in H_2O [8], a process governed by the basic photochemical reaction resulting from light–semiconductor interaction in the presence of water. In this approach, the semiconductor generates holes (h^+) in the valence band (VB) that oxidize H_2O near the surface and release protons (H^+; Eq. 1). Simultaneously, the electrons (e^-) promoted in the conduction band (CB) can reduce O_2 to generate different species, including superoxide radicals ($\cdot O_2^-$) and, subsequently, H_2O_2 by either a (i) single-electron indirect reduction and protonation (Eq. 2–4) or (ii) one-step two-electron direct O_2 reduction (Eq. 5).

$$2\,H_2O + 4\,h^+ \rightarrow O_2 + 4\,H^+ \quad \text{(Eq. 1)}$$

$$O_2 + e^- \rightarrow \cdot O_2^- \quad \text{(Eq. 2)}$$

$$\cdot O_2^- + H^+ \rightarrow HO_2\cdot \quad \text{(Eq. 3)}$$

$$HO_2\cdot + H^+ + e^- \rightarrow H_2O_2 \quad \text{(Eq. 4)}$$

$$O_2 + 2\,e^- + 2\,H^+ \rightarrow H_2O_2 \quad \text{(Eq. 5)}$$

ZnO [9] and TiO_2 [10-14] are the two major classical inorganic semiconductors used as photocatalysts [15, 16], among many others. Recently, carbon nitride with graphitic structure (g-C_3N_4) has emerged as a highly promising photocatalyst. Compared with classical metal-based semiconductors, it has a high efficiency and several advantages [17-20], the most attractive one being the absence of metal species known to decompose H_2O_2 via MOOH formation. Additionally, g-C_3N_4-based catalysts exhibit good photostability and photocatalytic activity under visible light. Finally, g-C_3N_4 can be prepared by the polycondensation and pyrolysis (500–600°C) of nitrogen- and carbon-containing precursors such as melamine and urea, both being cheap, abundant, and non-toxic in comparison with ZnO and TiO_2 [21]. However, pure carbon nitride has some bottlenecks limiting its photocatalytic efficiency, such as a fast electron–hole recombination of photogenerated species, insufficient absorption in visible light, a relatively large band gap (~2.7 eV), and a low specific surface area that limits the number of active sites for interfacial photoreactions. To address these issues, different strategies have been employed to enhance the photocatalytic activity, including non-metal doping (e.g., O [22, 23], P [24], N [25], and S [26]), metal ion doping (K [7], Cu [27]), forming heterojunctions with other semiconductors (e.g., ZnO [28], MnO_2 [29], and CeO_2 [30]), composites with metal nanoparticles (e.g., Au [20] and Ag [31]), and composites with carbonaceous materials (e.g., carbon dots [32], graphene [33], and carbon nanotubes [34]). The carbonaceous materials are selected as an electron transfer agent and photosensitizer in the photocatalysis field to reduce the electron–hole (e^-/h^+) recombination and to increase the absorption of incident light, respectively. Nowadays, the production of such functional carbon should avoid the use of non-renewable and fossil fuel-derived carbon precursors (e.g., polyacrylonitrile [PAN]), and instead use biosourced carbon. Cellulose nanofibers (CNF) are one

example, with 1–3 µm length and 5–10 nm width. They not only have the advantage of size but also possess adequate surface functional groups such as -OH and -COOH, facilitating regulation of the growth and chemical anchoring of chemical species such as precursors of inorganic photocatalysts [35]. Therefore, anchoring graphitic-like materials should be possible if they possess compatible functional groups. This implies the necessity of edge functional groups in g-C_3N_4 that possess H-bonding donor or acceptor ability.

Various research groups have already demonstrated the synergy of nanocellulose/g-C_3N_4 composites, with or without pyrolysis of the cellulose. It has led to the development of adsorbents or photocatalysts for the oxidation of dyes (methylene blue [36-39] or rhodamine [40, 41]), formaldehyde [42], Cr(IV) [43, 44], oil/water emulsion [45] or bacteria [46] and also the preparation of thermal insulator materials [47, 48]. These are promising routes especially for pollutant remediation; however, the future of photocatalysis also involves the production of chemicals by clean and low-energy processes. To the best of our knowledge, only one previous study used g-C_3N_4 and nanocellulose to produce an efficient photocatalyst to produce chemicals, H_2 in that case. However, nanocellulose was used only as a template to generate a chiral nematic structure in addition to the use of silica, with nanocellulose subsequently eliminated by calcination [49]. In our study, we used nanocellulose as both a template and a C-precursor to prepare a C/g-C_3N_4 composite by the simplest possible process. It is also worth mentioning the work by Jin et al., who used soluble cellulose acetate in combination with melamine as a g-C_3N_4 precursor to produce a C/g-C_3N_4 photocatalyst for the production of hydrogen [50].

In the present study, g-C_3N_4 nanosheets (CN2) were fabricated for the first time using a mixture of melamine and urea and a two-step calcination method, to generate a higher proportion of amino groups (-NH_x) than that in g-C_3N_4 prepared with only melamine (CN1); see Scheme 1 for the summary of the general strategy. We found that the as-prepared g-C_3N_4 nanosheets can easily and strongly bind the CNF, possibly by hydrogen or even covalent bonds. The cellulose nanofiber/g-C_3N_4 composite is then transformed by pyrolysis into a covalent heterojunction C/g-C_3N_4 (CNCF1 or

CNCF2) with consequences on the band structure and electron transfer process and an important improvement in the photocatalytic activity. As usual when designing a nanocomposite, apart from the nature of the interaction between the components, their mass ratio is an important factor. Prior experiments demonstrated that the optimum mass ratio of the cellulose nanofiber/g-C_3N_4 is ~3–4 %; therefore, this ratio was implemented throughout this study.

2. Experimental

2.1 Materials and reagents

Melamine ($C_3H_6N_6$; 99%), urea (CH_4N_2O; 99.5%), potassium dihydrogen phosphate (KH_2PO_4; 99.5%), potassium hydrogen phosphate (K_2HPO_4; 99%), N,N-Diethyl-p-phenylenediamine sulfate (DPD; 98%), horseradish peroxidase (POD; enzymatic activity >160 units/mg), anhydrous ethanol (AR), 5,5-dimethyl-1-pyrroline N-oxide (DMPO, 97%) were obtained from Aladdin Industrial Co., Ltd, China. Cellulose nanofibers (1 wt% aqueous solution; average length: 1–3 um, average width: 5–10 nm) was purchased from Guilin Qihong Technology Co., Ltd., China. Polyethersulfone (PES) membrane (∅ 13 mm × 0.22 μm) was obtained from Jin Teng Experimental Equipment Co., Ltd., Tianjin, China. All the chemical reagents mentioned above were of analytical grade and were utilized without further purification.

2.2 Preparation of photocatalysts

The g-C_3N_4 nanosheets were synthesized by a two-step pyrolysis treatment of melamine and urea [51]. First, melamine (3.2 g) and urea (0.8 g) were uniformly mixed and thoroughly ground in an agate mortar. The samples were placed into a muffle furnace and heated to 500°C with a heating rate of 2°C min^{-1} in static air and left for 2 h; then, the temperature was risen to 520°C for 2 h at the heating rate of 2°C min^{-1}. The residual yellow solids were ground into powder and calcined at 520°C for 4.5 h in air. Finally, the resultant light-yellow products with a productivity of 30% were denoted as CN2. For comparison, g-C_3N_4 nanosheets from a single precursor

was also synthesized by calcining pure melamine through the same thermal treatment and denoted as CN1, with a productivity of 36%.

The g-C_3N_4 composited with nanocarbon fibers was prepared by a one-step thermal treatment of the compound of g-C_3N_4 and CNF. In brief, g-C_3N_4 nanosheets (CN1 or CN2; 0.10 g) was added into 10 mL of deionized water containing a suspension of CNF (0.33 g; CNF concentration 1 wt%) and ultrasonicated for 30 min, as shown in Figure S1. Subsequently, the mixtures were vacuum-dried at 60°C for 12 h. Then, the residual white yellow solids were directly pyrolyzed at 500°C for 1 h at the heating rate of 5°C min^{-1} in argon atmosphere, marked as CNCFx (x = 1, 2). The final products (CNCF1 and CNCF2) obtained also retained the productivity of 80% and 70%, respectively. The pure CNF were carbonized into cellulosic carbon fibers, denoted as CF, under the same calcination conditions.

2.3 Characterization

The crystal structures of as-prepared samples were characterized using an X-ray diffractometer (Rigaku, Ultima IV, Japan) with Cu Ka radiation in the range between 5° and 80°. Fourier transform infrared (FTIR) spectra were recorded on a Bruker VERTEX 70 spectrophotometer at the wavelength ranging from 400 to 4000 cm^{-1}. The porosimetry measurements and BET-specific surface area of the samples was detected by nitrogen adsorption/desorption on an adsorption apparatus (Micromeritics, ASAP 2020, USA). The morphologies of the samples were observed using a scanning electron microscope (Hitachi, SU8010, Japan) and transmission electron microscope (JEOL, JEM-2100, Japan). The X-ray photoelectron spectrometer (XPS, ESCALAB 250, Thermo Scientific, USA) equipped with Al Kα radiation monochromatic source was used to detect chemical composition and elemental states. The ultraviolet (UV)-vis diffuse reflectance spectra (UV-vis DRS) were obtained using a UV-vis spectrophotometer (Cary 500, Varian, USA) in the range of 300–800 nm with $BaSO_4$ as a reflectance standard. Photoluminescence spectra were recorded on a LS55 spectrophotometer (Perkin-Elmer, USA) under the excitation wavelength of 365 nm at room temperature. Time-resolved photoluminescence (TRPL) spectra were obtained on a fluorescence spectrophotometer (FLS980, Edinburgh Instruments, UK). Photo-generated $\cdot O_2^-$ radical species in the photocatalytic process were detected with DMPO as a trapping agent. The absorbance of hydrogen peroxide solution was

determined by UV–visible spectrophotometer (US-Vis, Agilent 8453, USA) at the wavelength 551 nm.

2.4 Photoelectrochemical and electrochemical measurement

The transient photocurrent curves and electrochemical impedance spectroscopy were obtained on CHI660-E electrochemical workstation (Chenhua Instrument Company, Shanghai, China) based on a three-electrode cell composed of Pt wire as the counter electrode, Ag/AgCl electrode as the reference electrode, and fluorine-doped tin oxide (FTO) glass (1×1 cm^2) as the working electrode. Na_2SO_4 aqueous solution (0.2 mol/L) was used as the electrolyte. Five milligrams of the sample (CNx or CNCFx) was added to 1 mL of Nafion solution (0.5%) under ultrasonication for 30 min, and then deposited onto the FTO glass. The as-prepared working electrode was dried at 80°C for 3 h. The photoelectrochemical measurement was performed under visible light irradiation (Xe arc lamp: 300 W, the distance between the surface of the solution and light filter: 10 cm, filter wavelength: $\lambda > 420$ nm). The transient photocurrent was collected with the light on and off. The electrochemical impedance spectroscopy (EIS) was tested at the frequency of 0.01 and 10^6 Hz with the alternating current amplitude of 5 mV.

Rotating disk electrode (RDE) tests were also taken on a CHI660-E electrochemical workstation with a modulated speed rotator and a glassy carbon disk electrode (working electrode). The Ag/AgCl electrode and Pt wire electrode were used as the reference electrode and counter electrode, respectively. Two milligrams of the photocatalyst was dispersed into 1 mL of Nafion solution (10%) under ultrasonication for 30 min. Then, 10 μL of the suspension was dropped on a glassy carbon electrode with a diameter of 5 mm and air-dried at room temperature as the working electrode. The linear sweep voltammetry (LSV) curves were obtained using a phosphate buffer solution (0.1 mmol/L; pH 7) with O_2-saturated purging at a scanning rate of 10 mV/s and the rotating speed between 0 and 2500 rpm.

2.5 Photocatalytic activity measurements

For evaluating the photocatalytic H_2O_2 generation, the catalyst powder (50 mg) was dispersed in a solution of deionized water (45 mL) and ethanol (5 mL). Then, the suspension was ultrasonicated for 5 min and purged with O_2 gas for 30 min prior to visible irradiation. Then, the photocatalytic performance was examined under visible

light irradiation (Xe arc lamp: 300 W, the distance between surface f the solution and light filter: 10 cm, filter wavelength: $\lambda > 420$ nm) with continuous O_2 purging and stirring for 6 h. Every hour, an aliquot of the suspension (4 mL) was taken and filtered to remove the catalysts. The concentration of H_2O_2 was measured by a colorimetric method. To this end, 5 mL of the filtered solution was immediately mixed with 0.5 mL of phosphate buffer (0.5 M K_2HPO_4 and 0.5 M KH_2PO_4), DPD solution (50 µL), and peroxidase (50 µL), with vigorous shaking for 30 s. Then, the absorbance of the aqueous solution was measured at 551 nm using a UV–visible spectrophotometer [52].

The decomposition behavior of H_2O_2 with photocatalysts was investigated by adding 50 mg of the samples to 50 mL of H_2O_2 solution (1 mmol/L) with continuous stirring under visible light irradiation for 1 h. The stability of the as-prepared samples was evaluated by performing three consecutive tests. When finishing each run, the photocatalyst was collected using membrane filtration and washed with deionized water, then vacuum-dried at 50°C overnight, finally reused in the next cycle under the same conditions. Photocatalytic H_2O_2 concentration was also investigated by measuring the absorbance of the filtrate according to the Beer–Lambert law [52].

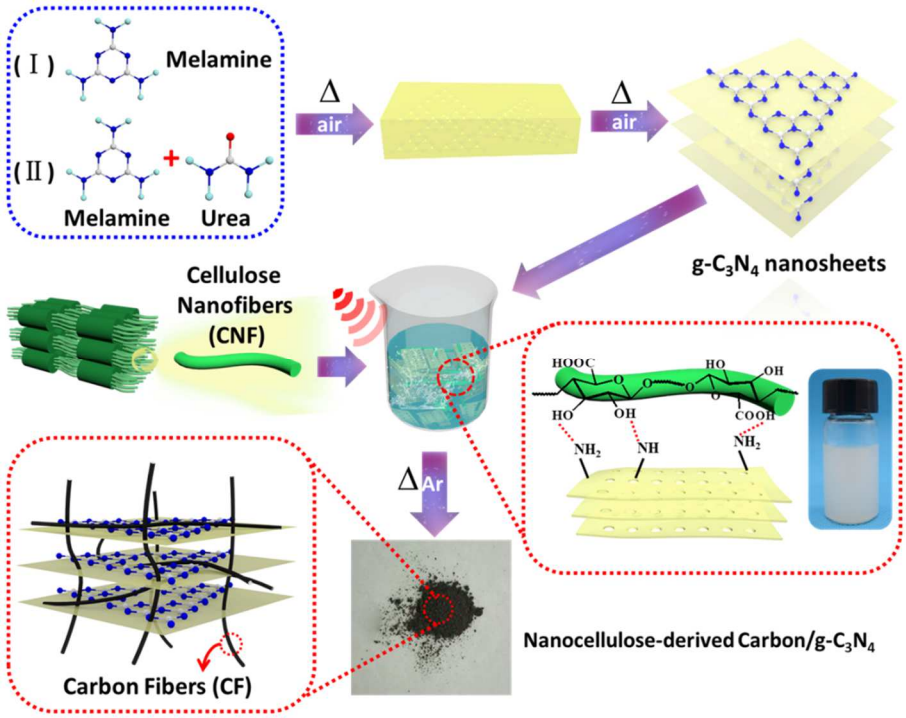

Scheme 1. Procedures for sample synthesis

3. Results and discussion

3.1 Photocatalyst preparation and characterization

Specific surface area is important for the activity of a photocatalyst; therefore, a bi-component approach was selected to prepare g-C_3N_4 with the highest possible surface area [53, 54]. Urea was used as an additive to melamine owing to the release of large quantities of volatile gas during thermal treatment, resulting in high porosity [55, 56]. It also can generate a high quantity of residual amino groups, generally on the edges of the nanosheets. Because CNF have surface -OH and -COOH groups, H-bonding and formation of amide or ester groups can occur through reactions with amino-rich carbon nitride. For comparison, a g-C_3N_4 was prepared by the mono-component approach using only melamine, which is referred to as CN1. A comparison between the dispersal behaviors of CN1 and CN2 with CNF in aqueous phase is shown in Figure S1, suggesting a higher stabilization of the suspension in the case of CNF/CN2 mixture.

Carbonization at 500°C of the CNF/CN1 and CNF/CN2 mixtures transforms their CNF into carbon, generating porosity throughout the materials and modifying the hydrophilic/hydrophobic balance of the surface in the corresponding CNCF1 and CNCF2, as shown in Figure S2. The results show that the CN2 (from dual precursors) was more hydrophilic than CN1 (from single precursor) owing to the presence of more hydrophilic groups (amino groups) in CN2. Moreover, the contact angles of CN1 (24.5^o) and CN2 (20.5^o) respectively decreased to 17.6^o (CNCF1) and 11^o (CNCF2) when g-C_3N_4 assembled with the carbon nanofibers pyrolyzed from nanocellulose was used, because of the increase in the stacking distance in g-C_3N_4. The optimized mass ratio of CNF/g-C_3N_4 is ~3.3 wt%, which is a miniscule quantity of CNF, but as shown below, it has a substantial effect on the photocatalytic performance compared with pure carbon nitride. Moreover, the sample yield is ~70–80% and with cheap and renewable products. This weight loss is attributed to the decomposition of cellulose and also the condensation reaction between the surface functional groups of cellulose and g-C_3N_4.

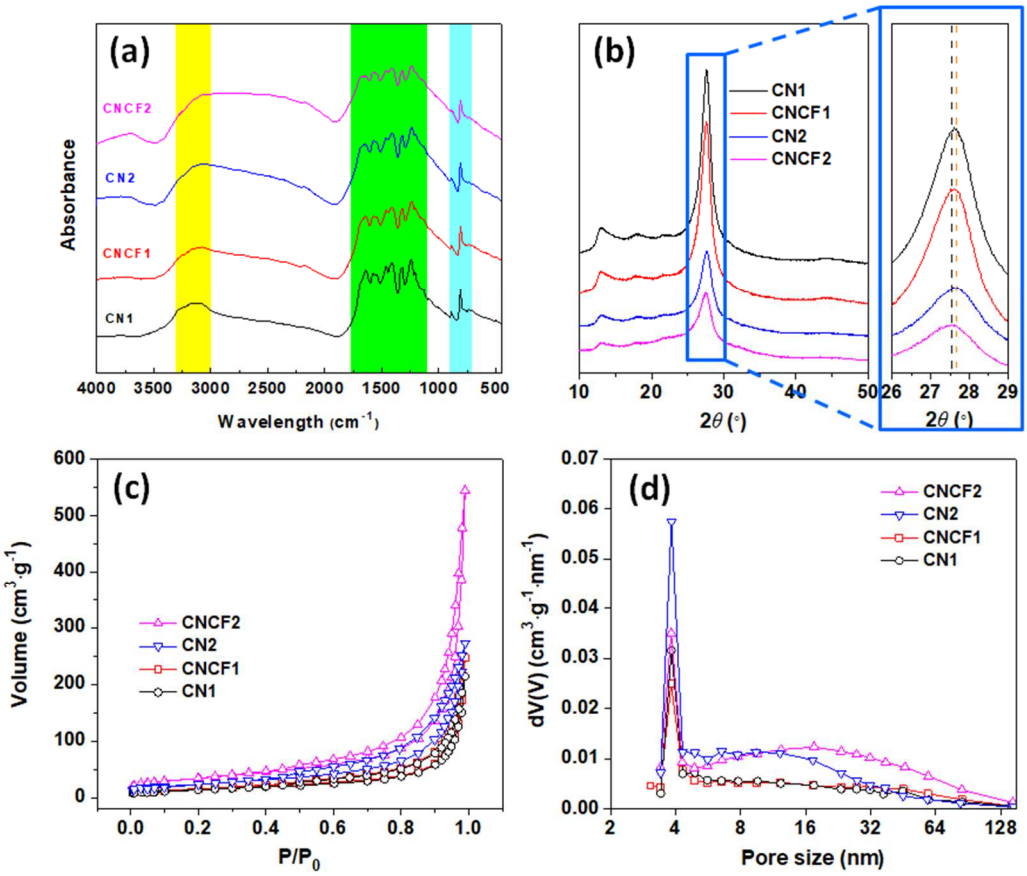

Figure 1. Fourier transform infrared spectroscopy curves (a), X-ray diffraction patterns (b), N_2 adsorption-desorption isotherms (c) and pore size distribution derived from desorption isotherm (d) of CN1, CN2, CNCF1, and CNCF2.

The generation of carbon results in an important modification of the color of the material from slightly yellow for pure carbon nitride (CN1 and CN2) to gray for CNCF1 and CNCF2, as shown in Figure S3. Analyzed by FT-IR (Figure 1a), all spectra of CNx and CNCFx (x = 1, 2) are dominated by the signals related to the presence of g-C_3N_4. Several strong bands in the 1200–1600 cm^{-1} region were typical for the stretching modes of the CN heterocycles [57]. The sharp peak at 810 cm^{-1} corresponds to the characteristic breathing vibration of tri-s-triazine units [58]. The broad bands ranging from 3000 cm^{-1} to 3300 cm^{-1} correspond to the NH and OH stretching vibrations [59]. The peak intensity of $–NH_x$ between 3000 cm^{-1} and 3300 cm^{-1} in CNCF1 and CNCF2 is slightly lower than that of CN1 and CN2, respectively; it implies a decrease in the number of amino groups [60].

279 The presence of g-C_3N_4 was also clearly detected in the signals observed in the
280 X-ray diffraction powder patterns of the CNx and CNCFx samples, as shown in
281 Figure 1b. The two characteristic peaks at 2θ = 12.9° and 27.5° are ascribed to the
282 (100) and (002) diffraction planes of the in-plane repeat tri-s-triazine units and the
283 interlayer stacking reflection of conjugated aromatic segments, respectively [61-63].
284 A slight downshift in the position of the (002) crystal plane was detected when
285 comparing CN1 and CN2 and CNCFx. It corresponds to a very small increase in the
286 stacking distance in g-C_3N_4 when assembled with the carbon nanofibers [64], possibly
287 owing to the intercalation of organic species during pyrolysis. A weaker peak intensity
288 of (002) was noted for CN2 and CNCF2 than for CN1 and CNCF1, respectively,
289 which may be ascribed to the effective exfoliation of g-C_3N_4 into sheet-like structures
290 by overcoming the weak van der Waals forces between layers in the calcination
291 process; this finding is consistent with other reports on g-C_3N_4 [65].
292 Porosity of the materials was determined by N_2 adsorption-desorption with the
293 isotherms shown in Figure 1c. All samples exhibited typical type IV isotherms with
294 H3 type hysteresis loops, indicating that the samples were micro-, meso-, and slightly
295 macroporous with a specific surface area of 50 $m^2 g^{-1}$ (CN1), 55 $m^2 g^{-1}$ (CNCF1), 83
296 $m^2 g^{-1}$ (CN2), and 120 $m^2 g^{-1}$ (CNCF2). The data emphasize the effect of CNF in
297 addition to the preparation method of g-C_3N_4. CN2 and CNCF2 exhibited 1.5–2.4
298 times higher BET SSA than CN1 and CNCF1 (Table S1). An increase was also
299 observed for the average pore volume, calculated to be 0.34 $m^3 g^{-1}$ (CN1), 0.39 $m^3 g^{-1}$
300 (CNCF1), 0.44 $m^3 g^{-1}$ (CN2), and 0.85 $m^3 g^{-1}$ (CNCF2; Table S1). Clearly, the
301 bi-component route results in materials with enhanced porosity that is ascribed to a
302 higher proportion of CO_2 and NH_3 release during calcination [66]. Notably, the
303 assembly of CNF with CN1 or CN2 leads to a decrease in the number of small
304 mesopores and an increase in the number of large mesopores increased, which is
305 expected when considering the formation of carbonaceous residue upon pyrolysis of
306 CNF (Figure 1d).

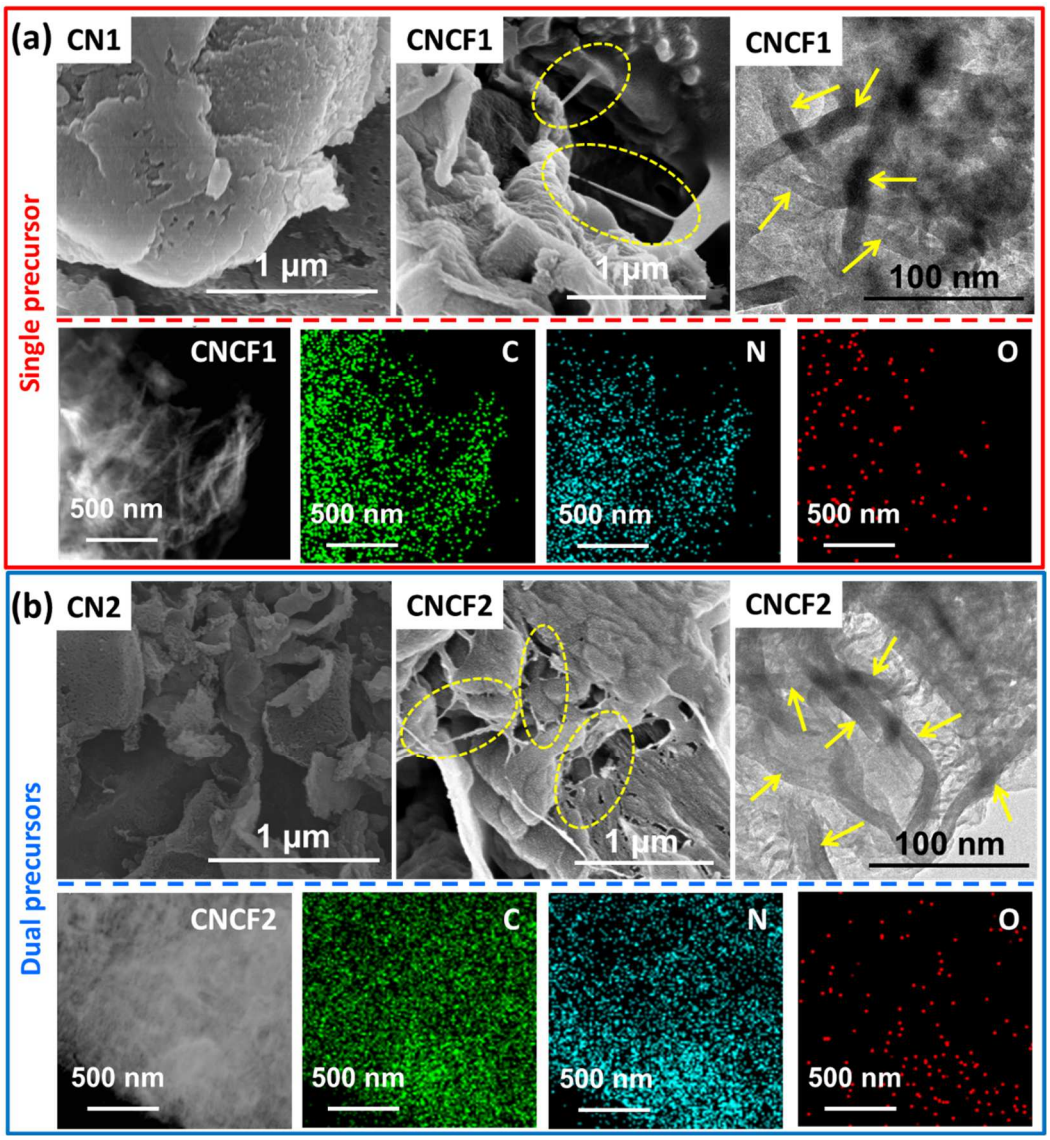

Figure 2. Scanning electron microscopy (SEM) images of CN1 and CNCF1; transmission electron microscopy (TEM) and TEM mapping of CNCF1 (a), SEM images of CN2 and CNCF2; TEM and TEM mapping of CNCF2 (b).

Scanning electron microscopy (SEM) and transmission electron microscopy (TEM) revealed the morphology and microstructure of CNx and CNCFx (x = 1 or 2). As shown in Figure 2, CN1 and CN2 are mainly composed of stacked irregular nanosheets. Compared with CN1, a thinner sheet-like structure was obtained for CN2 upon calcination. For samples after pyrolysis (CNCF1 and CNCF2), carbon nanofibers with an average length of 0.1–1 μm were identified on top of or between micron-sized layers of carbon nitride. Sheet-like carbon nitride particles of 8–12 μm

width were observed by TEM (Figure 2), suggesting that the assembly also occurs at the nanometer scale because isolated carbon nanofibers ∅ ≈ 10–20 nm were identified. This clearly showcases the integration of the CNF within the g-C_3N_4 during the assembly prior to pyrolysis. Elemental mapping by TEM shows that C and N, the two main elements of carbon nitride, are uniformly spread in CNCF1 and CNCF2, and only traces of oxygen are likewise distributed (Figure 2).

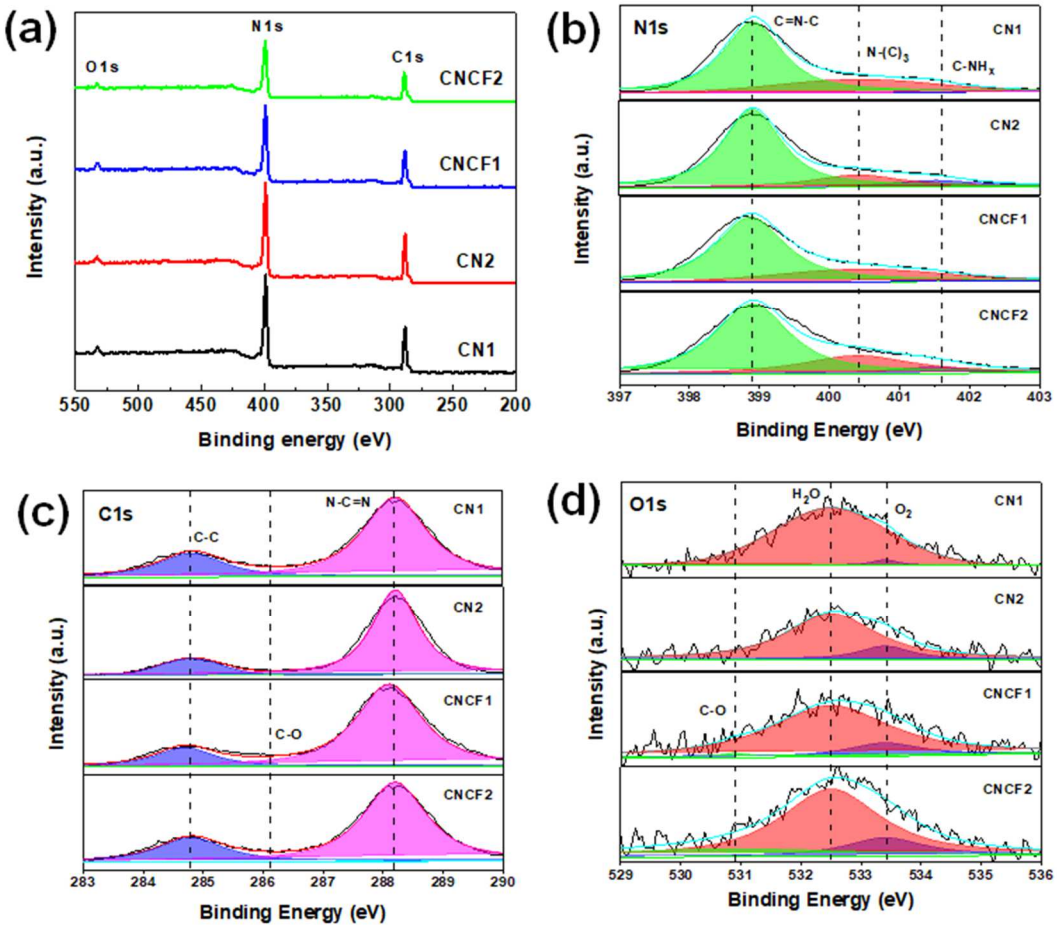

Figure 3. X-ray photoelectron spectroscopy data of CN1, CN2, CNCF1, and CNCF2 samples: survey scan (a), core spectra with deconvolution for N1s (b), C1s (c), and O1s (d).

X-ray photoelectron spectroscopy (XPS) allowed us to identify the composition and chemical status of the main elements in the samples (Figure 3). As shown in Figure 3a, similar X-ray photoelectron spectra were recorded for the four samples exhibiting the two peaks expected for g-C_3N_4, namely N 1s and C 1s and a weak signal of O 1s [67]. For N 1s spectra in Figure 3b, the three peaks at 398.9, 400.4, and

401.5 eV are assigned to sp^2-hybridized nitrogen (C=N-C), tertiary nitrogen (N-$(C_x)_3$) and C-NH_x, respectively [41]. An estimate of the relative proportion of the different species was obtained by deconvolution (Table S2). It appears that the percentage of C-NH_x either in CN2 or CNCF2 prepared by the bi-component route is considerably higher than that for the materials prepared by the mono-component route (CN1 and CNCF1). This is an additional indication of the effect of the urea precursor during the formation of the materials, and it is consistent with the FT-IR data [68] (Figure 1a). Moreover, the content of C-NH_x decreased after g-C_3N_4 was assembled and pyrolyzed with CNF, a possible explanation being the reaction of this amino group with the functional groups of cellulose (hydroxyl and carboxylic group) during assembly or with gaseous products issued from the decomposition of cellulose during pyrolysis.

In Figure 3c, C 1s spectrum could be deconvoluted into two peaks at 284.8 and 288.2 eV. The peak at 288.2 eV represents by far the highest proportion of C species and was attributed to sp^2-hybridized carbon covalently bound by N atom (N=C-N), as expected for g-C_3N_4. The peak at 284.8 eV was assigned to C-C carbon species [69], both routes of preparation led to a similar quantity of this species, indicating the presence of carbonaceous residue. With the assembly and pyrolysis of CNF, the content of N-C=N decreased by a few percent and that of C-C increased by 10% for CNCF1, which is expected because the pyrolysis of CNF leads to the formation of carbonaceous char that can adsorb on the surface of g-C_3N_4. However, this increase was not observed when comparing CN2 and CNCF2 and is attributable to a higher integration of the carbon fiber into the sheet-like structure of g-C_3N_4. C 1s XPS data also revealed a peak at 286.1 eV for CNCF1 and CNCF2, which was ascribed to C-O [70] that likely results from the assembly and pyrolysis with CNF, which generates O-containing carbon as observed in carbon-derived polysaccharides [71]. However, different routes of preparation resulted in different C-O content: 1–2% in CNCF1 versus 4–5 % for CNCF2. Concerning oxygen, the high-resolution O 1s spectra was fitted based on two reference peaks centered at binding energies of 533.4 eV and 532.5 eV for adsorbed O_2 and adsorbed H_2O, respectively [72]. Compared with the as-prepared g-C_3N_4 samples CN1 and CN2, the new peak at 530.9 eV in

CNF-modified g-C_3N_4 samples (CNCF1 and CNCF2) was ascribed to C-O [73]. These data are consistent with the C-O content observed on the C1 XPS spectra, the proportion of O in C-O species being 1–2% in CNCF1 and 3–4 % in CNCF2.

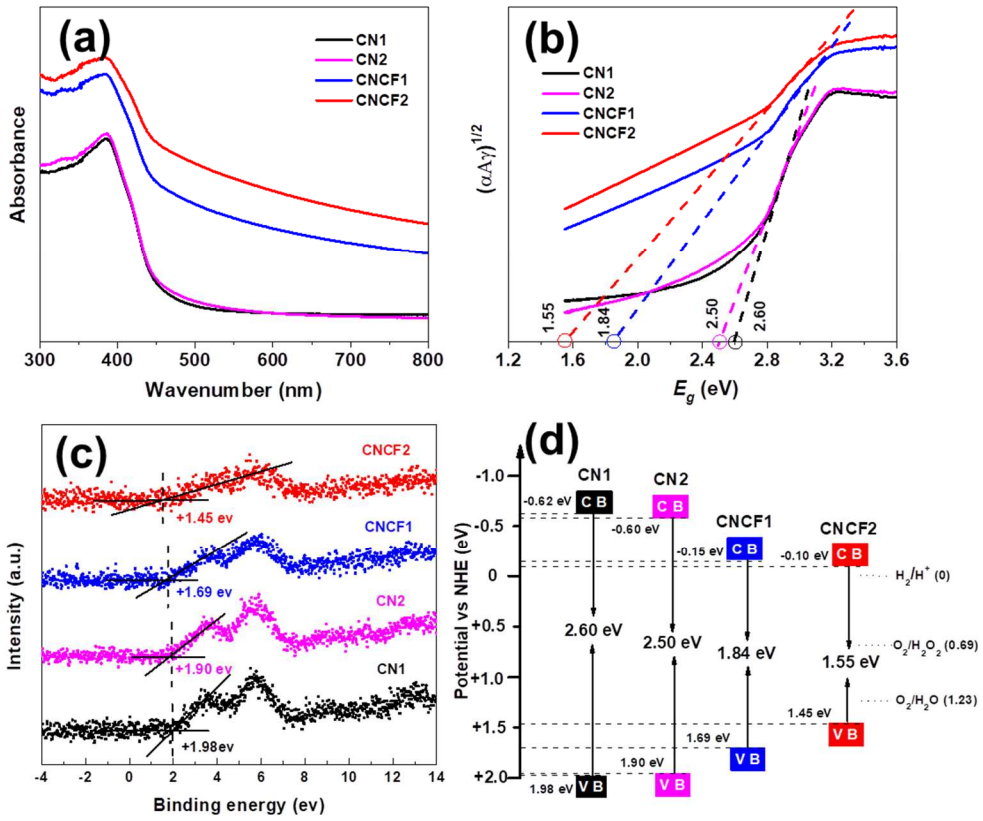

Figure 4. For CN1, CN2, CNCF1, and CNCF2: characterization by UV-vis DRS spectra (a), determination of the band gaps (b), determination of VB XPS spectra (c), and energy band structures (d)

To investigate the optical absorption and band structures, UV–visible diffuse reflectance spectra (UV-vis DRS) of the samples were recorded (Figure 4a). All samples presented absorption in the blue region typical of the 2D structure of carbon nitride [74]. However, compared with CN1 and CN2, the absorption intensity of both CNCF1 and CNCF2 was significantly increased owing to the presence of carbon fibers and multiple reflection of incident ray light across porous structures and band structure regulation [75]. The corresponding band gaps determined from Tauc's plots were 2.60, 2.50, 1.84, and 1.55 eV for CN1, CN2, CNCF1, and CNCF2, respectively

(Figure 4b). Therefore, the CNCF1 and CNCF2 samples exhibited a narrower band gap than other samples and consequently higher absorption of visible light useful in photogenerating carriers. The band structures of different samples were further investigated by VB XPS spectra as shown in Figure 4c. An additional effect of the presence of carbon fibers is the variation of the VB potential; values for CN1 (1.98 eV) and CN2 (1.90 eV) were decreased for CNCF1 (1.69 eV) and CNCF2 (1.45 eV). A decrease in the VB potential is beneficial in narrowing the band gap and decreasing the generation of ·OH because of the decreased oxidation ability. Combining the VB XPS spectra (Figure 4c), the location of VB and CB bands was determined using the formula $E_g = E_{VB} - E_{CB}$ (where E_g: band gap, E_{VB}: VB value, E_{CB}: CB value; Figure 4d). The E_g of CNCF1 and CNCF2 was smaller than that of CN1 and CN2, respectively. Importantly, the E_g is the smallest for CNCF2, which also has a more positive CB level (-0.1 eV vs NHE) than other samples, which is 0.79 eV more negative than the reduction potential of O_2/H_2O_2 (0.69 eV) and large enough to reduce O_2 to H_2O_2 [76]. Moreover, the positive shift of CB could easily trigger photogenerated electrons from CB, accepting electrons from carbon fibers and enhancing the two-electron reduction of O_2 to H_2O_2 [77, 78].

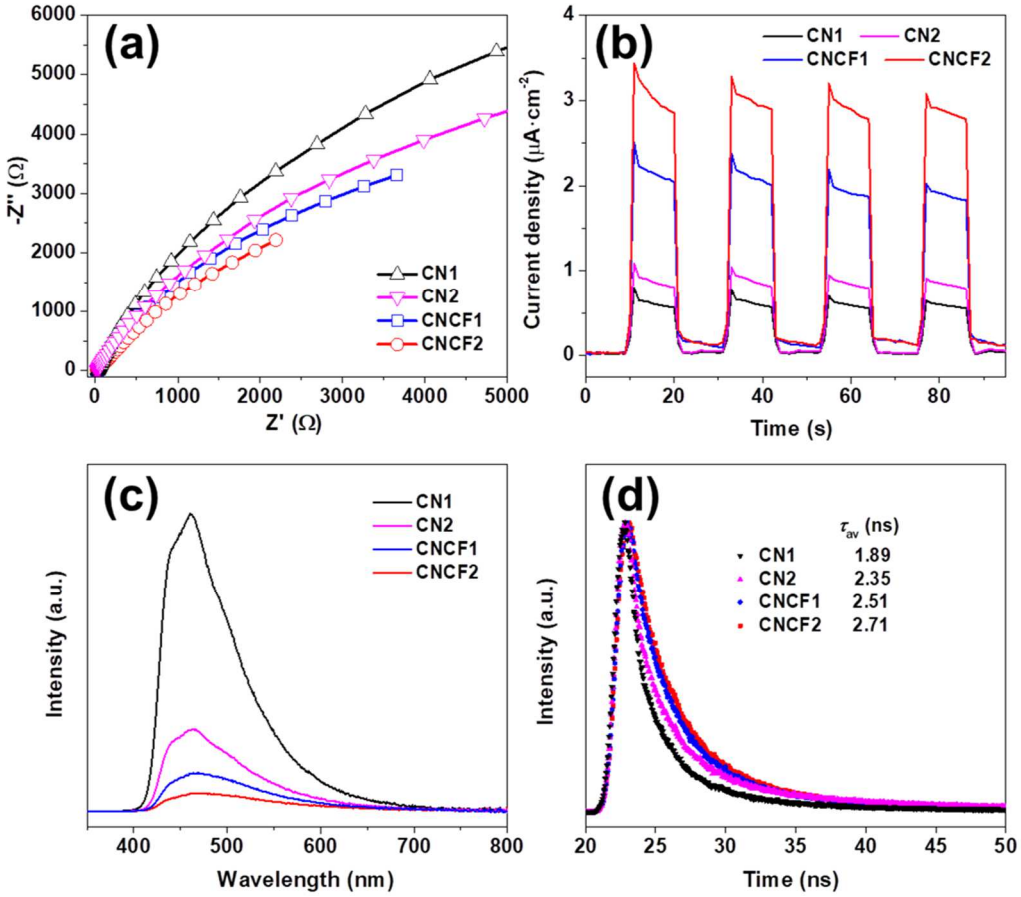

Figure 5. Electrochemical impedance spectra: Nyquist plots (a), transient photocurrent response curves (b), photoluminescence spectra (c), time-resolved photoluminescence decay spectra (d) of the samples.

Electrochemical impedance spectroscopy (EIS) was further employed to understand the charge separation and their transfer. As shown in Figure 5a, the Nyquist plots revealed that under visible light irradiation, the observed arc radius of CNCFx is smaller than the corresponding CNx, which indicates that the charge transfer resistance of CNCFx is significantly decreased. This is ascribed to the introduction of carbon nanofibers and carbonaceous residue that enhance electron transfer. The smaller arc radius of CNCF2 than CNCF1 indicates a faster charge transfer and a better efficiency of electron–hole separation. The transient photocurrent curves under visible light irradiation of the as-prepared samples are shown in Figure 5b. CNCF1 and CNCF2 displayed much higher photocurrent than that of CN1 and CN2, confirming that carbon fibers derived from nanocellulose accelerate electron

transfer. The recombination/separation of photogenerated species was investigated by photoluminescence (PL) spectra of the samples (Figure 5c). As a general trend, the lower the photoluminescence peak intensity, the higher the efficiency of photogenerated electron-hole pairs. The strong fluorescence emission peaks of CN1 (462 nm) and CN2 (466 nm) were slightly red shifted to 470 nm and 469 nm for CNCF1 and CNCF2, respectively, which further confirms the band gap decrease [79]. CNCF1 and CNCF2 samples had considerably lower photoluminescence intensities than CN1 and CN2, respectively, suggesting better separation rate of electrons and holes. Moreover, it is worth noting that the photoluminescence quenching efficiency of CNCF2 was lower than CNCF1, suggesting more effective electron transfer from photogenerated g-C_3N_4 to nanocarbon fibers [74]. To obtain the average radiative lifetime of the recombining charge carriers, time-resolved photoluminescence (TRPL) characterization was investigated (Figure 5d). The average radiative lifetime (τ_{ave}) was further calculated according to the following equation: $\tau_{ave} = (B_1\tau_1^2 + B_2\tau_2^2)/(B_1\tau_1 + B_2\tau_2)$. The value of τ_{ave} for CN1 and CN2 was 1.89 and 2.35 ns, respectively, whereas that for CNCF1 and CNCF2 was 2.51 and 2.71 ns, respectively. This result indicated that, with the addition of carbon fibers derived from nanocellulose, the markedly extended lifetime of photogenerated charge carriers accelerates the charge separation efficiency. In summary, the presence of cellulose-derived carbon fibers assembled with g-C_3N_4 highly improved the efficiency of the photocatalysts in promoting charge transfer and carrier separation in g-C_3N_4.

3.2 Photocatalytic production of H_2O_2

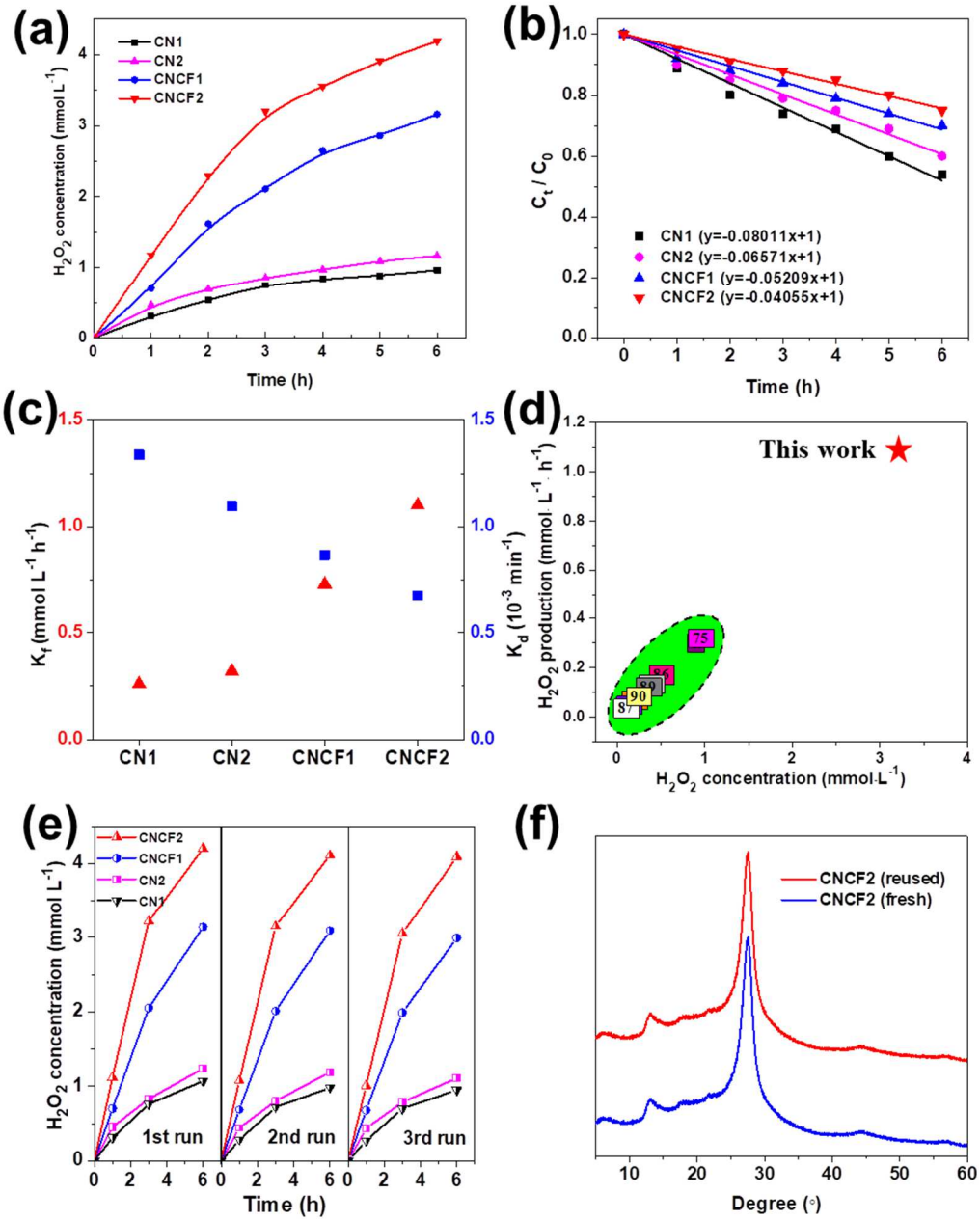

Figure 6. Photocatalytic production of H_2O_2 as a function of time under visible light with CN1, CN2, CNCF1, and CNCF2 as photocatalysts (a); photocatalytic decomposition of H_2O_2 under visible light irradiation (b); formation rate (K_f) and decomposition rate constant (K_d) for H_2O_2 photocatalytic production (c); comparison of reported photocatalytic performances (photocatalytic production rate of H_2O_2 within 3h and H_2O_2 concentration after 3h reaction) (d); reusability assessment of the different photocatalysts (e); X-ray diffraction patterns of CNCF2 before and after photocatalytic H_2O_2 production (f)

Photocatalytic production of H_2O_2 under visible light irradiation was evaluated by measuring the quantity of H_2O_2 versus time of reaction under atmospheric pressure at 25 ± 0.1°C using a catalyst concentration of 1.00 ± 0.01 g L^{-1} (Figure 6a). Because ethanol is known to have a good effect on photocatalytic H_2O_2 production when used as a proton donor (Figure S4), 5 mL (85.9 mmol) ethanol was used in this photocatalytic system with an ethanol-to-water ratio of 1: 9 (v/v). With CN1, only 0.31 mmol L^{-1} of H_2O_2 is formed after 1 h. Although the productivity is improved with CN2, it remains low: 0.47 mmol L^{-1} of H_2O_2 after 1 h. CNCF1 and CNCF2 presented a considerably higher H_2O_2 productivity after 1 h, 0.7 mmol L^{-1} and 1.18 mmol L^{-1}, respectively. Therefore, the kinetic study presented in Figure 6c suggests that the order of photocatalytic efficiency is as follows: CNCF2 > CNCF1 > CN2 > CN1.

The decomposition behavior of H_2O_2 was investigated under visible light irradiation with photocatalysts and a H_2O_2 concentration =1 mmol L^{-1}. As shown in Figure 6b, the level of H_2O_2 decomposition was ~8% and ~5% with CNCF1 and CNCF2, respectively, after 1 h of visible light irradiation, which was lower than that with CN1 and CN2 (~10%). The H_2O_2 decomposition rate constant (K_d) was calculated with the following equation: $K_d = -\ln(C_t/C_0)/t$, where C_t is the H_2O_2 concentration at time t, and C_0 is the initial concentration of H_2O_2 (1 mmol L^{-1}). Figure 6c shows that the K_d of CN1 (1.335×10^{-3} min^{-1}) and CN2 (1.095×10^{-3} min^{-1}) was higher than that of CNCF1 (0.868×10^{-3} min^{-1}) and CNCF2 (0.676×10^{-3} min^{-1}). These results confirm that carbon fibers derived from nanocellulose effectively inhibit the decomposition of H_2O_2 on carbon nitride.

Compared with previously reported values [7, 75, 80-86], the photocatalyst CNCF2 presented a significantly improved activity (Figure 6d). To investigate the recyclability of the as-prepared photocatalysts, after 6 h of reaction time, the catalyst was separated and washed from the suspension by filtration and then used again in a new batch of H_2O_2 production under the same conditions (Figure 6e). After three cycles, the photocatalyst was almost unchanged and the photocatalytic activity was

maintained. The X-ray diffraction analysis showed that both the fresh and reused CNCF2 catalysts exhibited almost the same typical peaks, as shown in Figure 6f.

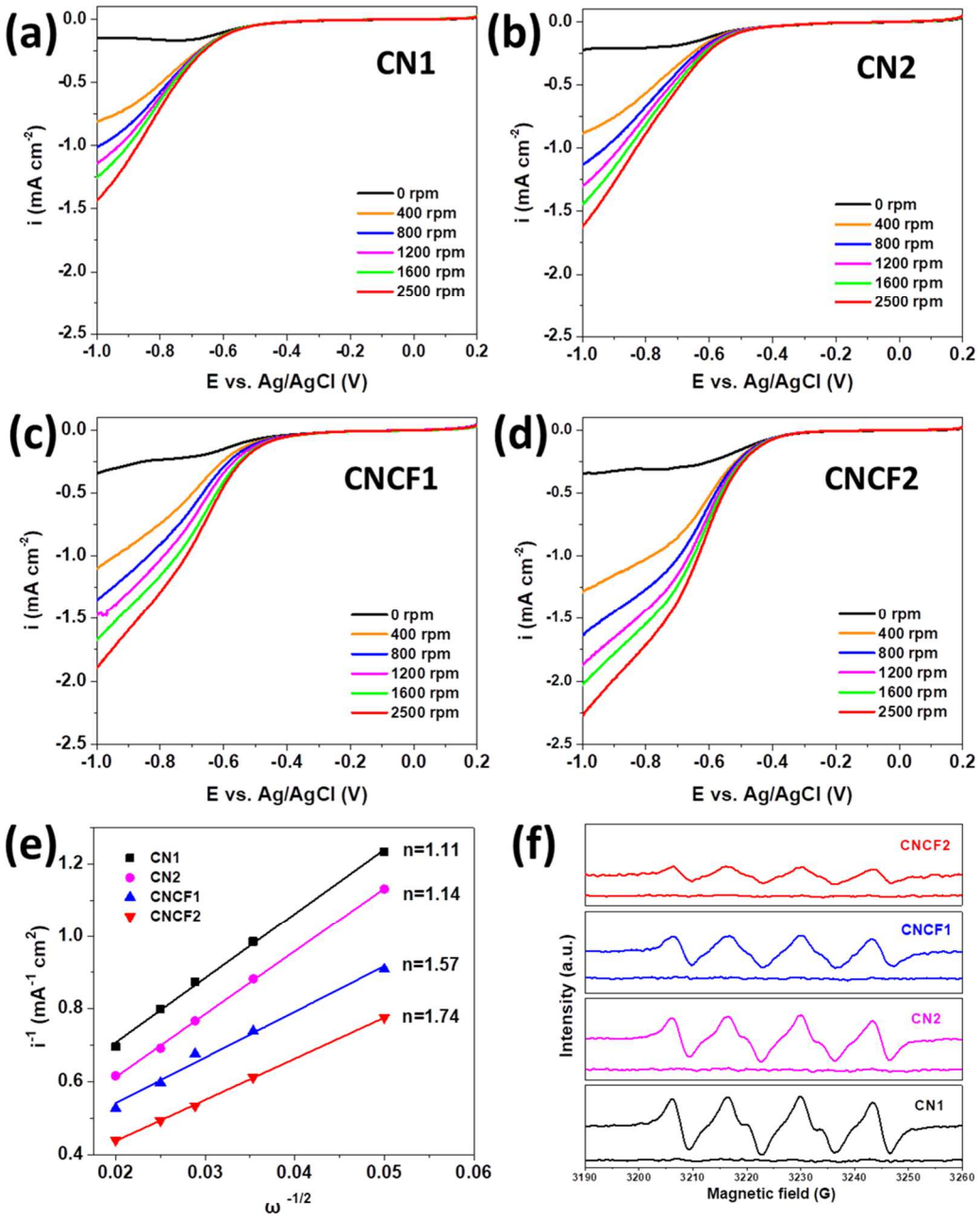

Figure 7. Linear sweep voltammetry curves of CN1 (a), CN2 (b), CNCF1 (c) and CNCF2 (d) measured on a rotating disk electrode at different rotating speeds; Koutecky-Levich plots of the data obtained at a constant electrode potential (-1.0 V vs. Ag/AgCl) (e), Electron paramagnetic resonance spectra of the DMPO-·O_2^- adduct (f)

To further investigate the O_2 reduction pathway, a rotating disk electrode (RDE) analysis of the O_2 reduction reaction (ORR) was performed. The linear sweep voltammetry (LSV) curves in Figure 7a-d for the as-prepared samples were measured by an RDE in phosphate buffer solution (0.1 mol L^{-1}, pH = 7) at different rotating speeds. The Koutecky-Levich plots derived from the LSV data are presented in Figure 7e. The average number of transfer electrons was calculated using the following equations:

$$j^{-1} = j_k^{-1} + B^{-1}\omega^{-1/2}$$

$$B = 0.2nFv^{-1/6}CD^{2/3}$$

, where j is the current density, j_k is the kinetic current density, ω is the rotating speed, F is the Faraday constant (96485 C mol^{-1}), v is the kinetic viscosity of water (0.01 cm^2 s^{-1}), and C is the O_2 concentration in water (1.26×10^{-5} cm^2 s^{-1}). The average number of electrons (n) was 1.11 and 1.14 for CN1 and CN2, respectively, and 1.57 and 1.74 for CNCF1 and CNCF2, respectively. These results suggest that single-electron O_2 reduction occurs on CN1 and CN2 because the n value of CN1 and CN2 was approximately 1. In contrast, the average number of electrons is above 1.5 when nanocellulose-derived carbon is present, especially for CNCF2, for which an O_2 reduction by two-electron process is likely. Thus, the ORR for CNCF1 and CNCF2 had a hybrid single/two-electron function, whereas that for CN1 and CN2 showed only single-electron function.

Electron paramagnetic resonance (EPR) analysis with DMPO as a trapping agent of $\cdot O_2^-$ was performed to identify the pathway of conversion of molecular oxygen to H_2O_2. As shown in Figure 7f, the characteristic peaks of DMPO-$\cdot O_2^-$ were observed in all samples, indicating that $\cdot O_2^-$ was generated as an intermediate in the formation of H_2O_2. As seen in Figure 7f, CN1 and CN2 both presented higher-intensity EPR signals than CNCF1 and CNCF2, indicating that CN1 and CN2 generate more $\cdot O_2^-$ than CNCF1 and CNCF2. The finding implies that reduction of O_2 into $\cdot O_2^-$ occurs on the four samples by a single-electron pathway leading to H_2O_2 formation. It is interesting that, CNCF1 and CNCF2 present partial O_2 directly reduction into H_2O_2 by a two-electron pathway[87]. Scheme 2 illustrates photocatalytic H_2O_2 production

by nanocellulose-derived C/g-C_3N_4 nano-heterojunction. Cellulose nanofibers with -OH and -COOH groups can bind to carbon nitride with intrinsic amino groups (-NH, -NH_2) and thermally transform into an effective heterojunction, increasing the linking between g-C_3N_4 nanosheets and carbon fibers. Furthermore, the carbon fibers reduce the band gap and greatly increase the electron transfer during the photocatalytic reaction. The photocatalytic efficiency also depends on the capacity and strength of adsorption of molecular oxygen onto the surface of carbon nitride. By porosimetrie, BET SSA of CN2 is 2.2 times higher than that of CN1 (Table S1), which provides more space and active sites to adsorb oxygen molecules [88]. The adsorption strength of molecular oxygen is also potentially reinforced by the presence of N atoms of amino groups in CN2, which are able to bind to oxygen as a Lewis acid [89]. As previously reported, such adsorption of oxygen on the surface of the photocatalyst catalyst is highly beneficial to the electron transfer [90]. An exciting point is to observe that with the presence of carbon nanofiber, the EPR intensity of $\cdot O_2^-$ of CNCF1 is higher than CNCF2. The data demonstrate the interest of the bi-component synthetic route chosen for the preparation of the g-C_3N_4. This is ascribed to both the larger BET specific surface area and the specific photophysical properties.

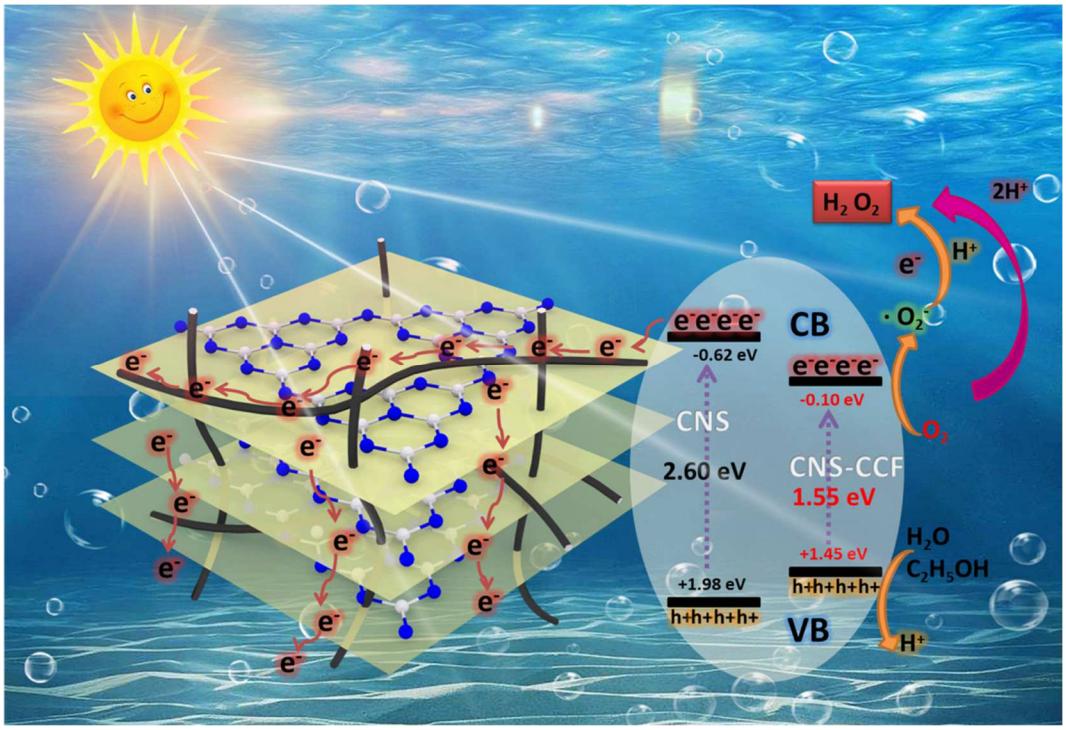

Scheme 2. Role of cellulosic carbon fibers for photocatalytic H_2O_2 production photocatalyzed by a nanocellulose-derived carbon/g-C_3N_4 nanocomposite.

4. Conclusions

The high improvement of the photocatalytic production of hydrogen peroxide (H_2O_2) over carbon nitride (g-C_3N_4) that we report is ascribable of main major phenomenon. First, we show that the presence of a very low content of nanocellulose-derived carbon deeply modify the photoactivity of the g-C_3N_4 assembled with it. The result is an outstanding photocatalytic H_2O_2 production of 1.10 mmol L^{-1} h^{-1} under visible light. The second critical point is to achieve a high level of interaction between the g-C_3N_4 nanosheets and CNF when assembling these two nanocomponents. Third, a high level of interaction can be achieved through the preparation of amino-rich g-C_3N_4 using a bi-component mixture of melamine and urea. When carbon fibers are closely incorporated into the stacked structure of g-C_3N_4, the nanofibers not only improve the porosity of the materials but also have a strong effect on the photophysical properties of the g-C_3N_4 in narrowing the band gap; improving the visible light absorption; increasing the number of photogenerated carriers, especially excitable electrons; and accelerating the electron transfer and further promoting a direct two-electron O_2 reduction reaction to generate hydrogen peroxide. In subsequent studies, this approach will be tested for other materials for the photoproduction of other chemicals.

Acknowledgments

This work was supported by the Project Funded by China Postdoctoral Science Foundation (2020T130215), Key Laboratory of State Forestry and Grassland Ministry (2019KFJJ16), Distinguished Young Talents of Fujian Agriculture and Forestry University (XJQ201806), Science and Technology Innovation Fund of Fujian Agriculture and Forestry University (CXZX2018013), and Fujian Innovation and Entrepreneurship Training Program (S202010389078).

References

[1] W.C. Hou, Y.S. Wang, ACS Sustainable Chemistry & Engineering 5 (2017) 2994-3001.

[2] H. Hou, X. Zeng, X. Zhang, Angewandte Chemie-International Edition 59 (2019) 17356-17376.

[3] Y. Yang, R.Z. Dong, Y.L. Zhu, H.S. Li, H. Zhang, X.M. Fan, H.L. Chang, Chemical Engineering Journal 381 (2020) 122749.

[4] T. Kato, K. Yoshizawa, European Journal of Organic Chemistry 2011 (2011) 4113-4120.

[5] Y. Sun, L. Silvioli, N.R. Sahraie, W. Ju, J. Li, A. Zitolo, S. Li, A. Bagger, L. Arnarson, X. Wang, T. Moeller, D. Bernsmeier, J. Rossmeisl, F. Jaouen, P. Strasser, Journal of the American Chemical Society 141 (2019) 12372-12381.

[6] H. Hirakawa, S. Shiota, Y. Shiraishi, H. Sakamoto, S. Ichikawa, T. Hirai, ACS Catalysis 6 (2016) 4976-4982.

[7] S. Kim, G.-h. Moon, H. Kim, Y. Mun, P. Zhang, J. Lee, W. Choi, Journal of Catalysis 357 (2018) 51-58.

[8] L. Yang, G. Dong, D.L. Jacobs, Y. Wang, L. Zang, C. Wang, Journal of Catalysis 352 (2017) 274-281.

[9] C. Kormann, D.W. Bahnemann, M.R. Hoffmann, Environmental Science & Technology 22 (1988) 798-806.

[10] D. Tsukamoto, A. Shiro, Y. Shiraishi, Y. Sugano, S. Ichikawa, S. Tanaka, T. Hirai, ACS Catalysis 2 (2012) 599-603.

[11] T. Hirakawa, Y. Nosaka, The Journal of Physical Chemistry C 112 (2008) 15818-15823.

[12] M. Teranishi, S. Naya, H. Tada, Journal of the American Chemical Society 132 (2010) 7850-7851.

[13] H. Goto, Y. Hanada, T. Ohno, M. Matsumura, Journal of Catalysis 225 (2004) 223-229.

[14] L. Zheng, J. Zhang, Y.H. Hu, M. Long, The Journal of Physical Chemistry C 123 (2019) 13693-13701.

[15] S. Sun, X. Yu, Q. Yang, Z. Yang, S. Liang, Nanoscale Advances 1 (2019) 34-63.

[16] C. Ray, T. Pal, Journal of Materials Chemistry A 5 (2017) 9465-9487.

[17] Z. Haider, H.I. Cho, G.H. Moon, H.I. Kim, Catalysis Today 335 (2019) 55-64.

[18] Z. Li, N. Xiong, G. Gu, Dalton Transactions 48 (2019) 182-189.

[19] X. Li, J. Zhang, F. Zhou, H. Zhang, J. Bai, Y. Wang, H. Wang, Chinese Journal of Catalysis 39 (2018) 1090-1098.

[20] G.F. Zuo, S.S. Liu, L. Wang, H. Song, P.X. Zong, W.S. Hou, B.D. Li, Z.L. Guo, X.G. Meng, Y. Du, T. Wang, V.A.L. Roy, Catalysis Communication 123 (2019) 69-72.

[21] A. Thomas, A. Fischer, F. Goettmann, M. Antonietti, J.O. Muller, R. Schlogl, J.M. Carlsson, Journal of Materials Chemistry 18 (2008) 4893-4908.

[22] S. Samanta, R. Yadav, A. Kumar, A.K. Sinha, R. Srivastava, Applied Catalysis B-Environmental 259 (2019) 118054.

[23] H. Wang, Y.H. Guan, S.Z. Hu, Y.B. Pei, W.T. Ma, Z.P. Fan, Nano 14 (2019) 1950023.

[24] J. Tian, T.J. Wu, D. Wang, Y. Pei, M.H. Qiao, B.N. Zong, Catalysis Today 330 (2019) 171-178.

[25] X.Y. Qu, S.Z. Hu, P. Li, Z. Li, H. Wang, H.F. Ma, W. Li, Diamond and Related Materials 86 (2018) 159-166.

[26] L.H. Zheng, J.Z. Zhang, Y.H. Hu, M.C. Long, Journal of Physical Chemistry C 123 (2019) 13693-13701.

[27] S.Z. Hu, X.Y. Qu, P. Li, F. Wang, Q. Li, L.J. Song, Y.F. Zhao, X.X. Kang, Chemical Engineering Journal 334 (2018) 410-418.

[28] H.L. Tian, H.Q. Fan, J.W. Ma, L.T. Ma, G.Z. Dong, Electrochim Acta 247 (2017) 787-794.

[29] Y.J. Zhou, L. Li, Y.H. Wan, T.T. Chen, X. Chu, Analytic Methods 10 (2018) 5084-5090.

[30] W. Liu, J.B. Zhou, Z.S. Hu, Separation Purification Technology 227 (2019) 115665.

[31] Y.K. Wang, S.Z. Hu, Q. Li, G.Z. Gu, Y.F. Zhao, H.Y. Liang, W. Li, RSC Advances 8 (2018) 36903-36909.

[32] S. Asadzadeh-Khaneghah, A. Habibi-Yangjeh, K. Nakata, Journal of Photochemistry and Photobiology A-Chemistry 374 (2019) 161-172.

[33] D.L. Jiang, Y. Zhang, H.Y. Chu, J. Liu, J. Wan, M. Chen, RSC Advances 4 (2014) 16163-16171.

[34] S. Zhao, T. Guo, X. Li, T.G. Xu, B. Yang, X. Zhao, Applied Catalysis B-Environmental 224 (2018) 725-732.

[35] M.L. Foresti, A. Vázquez, B. Boury, Carbohydrate Polymers 157 (2017) 447-467.

[36] T. Dou, L. Zang, Y. Zhang, Z. Sun, L. Sun, C. Wang, Materials Letters 244 (2019) 151-154.

[37] H. Wang, J. Li, N. Ding, X. Zeng, X. Tang, Y. Sun, T. Lei, L. Lin, Chemical Engineering Journal 386 (2020) 124021.

[38] P. Yang, J. Wang, G. Yue, R. Yang, P. Zhao, L. Yang, X. Zhao, D. Astruc, Journal of Photochemistry and Photobiology A: Chemistry 388 (2019) 112169.

[39] W. Bai, X. Yang, X. Du, Z. Qian, Y. Zhang, L. Liu, J. Yao, Applied Surface Science 504 (2020) 144179.

[40] H. Zhao, S. Chen, X. Quan, H. Yu, H. Zhao, Applied Catalysis B: Environmental 194 (2016) 134-140.

[41] H. Qi, X. Ji, C. Shi, R. Ma, Z. Huang, M. Guo, J. Li, Z. Guo, Journal of Colloid Interface Science 556 (2019) 366-375.

[42] X. Li, X. Qian, X. An, J. Huang, Applied Surface Science 487 (2019) 1262-1270.

[43] S. Chen, W. Lu, J. Han, H. Zhong, T. Xu, G. Wang, W. Chen, Chemical Engineering Journal 359 (2019) 119-129.

[44] S. Wang, F. Li, X. Dai, C. Wang, X. Lv, G.I.N. Waterhouse, H. Fan, S. Ai, Journal of Hazardous Materials 384 (2020) 121417.

[45] F. Li, Z. Yu, H. Shi, Q. Yang, Q. Chen, Y. Pan, G. Zeng, L. Yan, Chemical Engineering Journal 322 (2017) 33-45.

[46] S.-W. Zhao, M. Zheng, H.-L. Sun, S.-J. Li, Q.-J. Pan, Y.-R. Guo, Dalton Transactions (2019) 3723-3734.

[47] B. Wu, L. Ge, H. Wu, X. Wang, Q. Ge, J. Miao, M. Cao, P. Chen, R. Xia, J. Qian, Advanced Materials Interfaces 6 (2019) 1801406.

[48] L. Mu, L. Shi, Y. Wang, Q. Zhou, J. Ye, X. Feng, Journal of Materials Chemistry C 6 (2018) 12660-12667.

[49] W.S. Lin, W. Hong, L. Sun, D. Yu, D.S. Yu, X.D. Chen, Chemsuschem 11 (2018) 114-119.

[50] Z. Jin, J. Chen, S. Huang, J. Wu, Q. Zhang, W. Zhang, Y.-J. Zeng, S. Ruan, T. Ohno, Catalysis Today 315 (2018) 149-154.

[51] Y. Li, R. Jin, Y. Xing, J. Li, S. Song, X. Liu, M. Li, R. Jin, Advanced Energy Materials 6 (2016) 1601273.

[52] L. Liu, W. Sun, W. Yang, Q. Li, J.K. Shang, Scientific Reports 6 (2016) 20878.

[53] F. Dong, Z. Zhao, T. Xiong, Z. Ni, W. Zhang, Y. Sun, W.-K. Ho, ACS Applied Materials & Interfaces 5 (2013) 11392-11401.

[54] F. Dong, Z. Ni, P. Li, Z. Wu, New Journal of Chemistry 39 (2015) 4737-4744.

[55] S. Martha, A. Nashim, K.M. Parida, Journal of Materials Chemistry A 1 (2013) 7816-7824.

[56] D.M. Ruan, S. Kim, M. Fujitsuka, T. Majima, Applied Catalysis B-Environmental 238 (2018) 638-646.

[57] J. Tian, D. Wang, S. Li, Y. Pei, M. Qao, Z.-H. Li, J. Zhang, B. Zong, ACS Sustainable Chemistry & Engineering 8 (2020) 594-603.

[58] Y.L. Li, P.P. Li, J.S. Wang, Y.L. Yang, W.Q. Yao, Z. Wei, J.S. Wu, X.X. Yan, X.F. Xu, Y.H. Liu, Y.F. Zhu, Applied Catalysis B-Environmental 225 (2018) 519-529.

[59] F. Dong, Z.Y. Wang, Y.J. Sun, W.K. Ho, H.D. Zhang, Journal of Colloid Interface Science 401 (2013) 70-79.

[60] H. Yu, R. Shi, Y. Zhao, T. Bian, Y. Zhao, C. Zhou, G.I.N. Waterhouse, L.Z. Wu, C.H. Tung, T. Zhang, Advanced Materials 29 (2017) 1605148.

[61] A.J. Cai, Q. Wang, Y.F. Chang, X.P. Wang, Journal of Alloys and Compounds 692 (2017) 183-189.

[62] Y. Yang, C. Zhang, D. Huang, G. Zeng, J. Huang, C. Lai, C. Zhou, W. Wang, H. Guo, W. Xue, R. Deng, M. Cheng, W. Xiong, Applied Catalysis B: Environmental 245 (2019) 87-99.

[63] J.S. Zhang, Y. Chen, X.C. Wang, Energy & Environmental Science 8 (2015) 3092-3108.

[64] P. Niu, H. Li, Y. Ma, T. Zhai, The Journal of Physical Chemistry C 122 (2018) 20717-20726.

[65] J. Xu, L. Zhang, R. Shi, Y. Zhu, Journal of Materials Chemistry A 1 (2013) 14766-14772.

[66] F. Dong, Z.W. Zhao, T. Xiong, Z.L. Ni, W.D. Zhang, Y.J. Sun, W.K. Ho, ACS Applied Materials Interfaces 5 (2013) 11392-11401.

[67] H.J. Li, B.W. Sun, L. Sui, D.J. Qian, M. Chen, Physical Chemistry Chemical Physics 17 (2015) 3309-3315.

[68] J. Zhang, F. Huang, Applied Surface Science 358 (2015) 287-295.

[69] L. Shi, L. Yang, W. Zhou, Y. Liu, L. Yin, X. Hai, H. Song, J. Ye, Small 14 (2018) 1703142.

[70] J.X. Huang, D.G. Li, R.B. Li, Q.X. Zhang, T.S. Chen, H.J. Liu, Y. Liu, W.Y. Lv, G.G. Liu, Chemical Engineering Journal 374 (2019) 242-253.

[71] P. Deng, H. Li, Z. Wang, Y. Hou, Applied Surface Science 504 (2020) 144454.

[72] F. Cheng, J. Yan, C. Zhou, B. Chen, P. Li, Z. Chen, X. Dong, Journal of Colloid Interface Science 468 (2016) 103-109.

[73]A. Sánchez-Sánchez, F. Suárez-García, A. Martínez-Alonso, J.M.D. Tascón, Carbon 70 (2014) 119-129.

[74] G. Wang, Y. Zhao, H. Ma, C. Zhang, X.Dong, X. Zhang. Science of The Total Environment 756 (2020) 144139.

[75] R. Wang, X. Zhang, F. Li, D. Cao, M. Pu, D. Han, J. Yang, X. Xiang, Journal of Energy Chemistry 27 (2018) 343-350.

[76] S. Zhao, X. Zhao, S. Ouyang, Y. Zhu, Catalysis Science & Technology 8 (2018) 1686-1695.

[77] D. Tsukamoto, A. Shiro, Y. Shiraishi, Y. Sugano, S. Ichikawa, S. Tanaka, T. Hirai, ACS Catalysis 2 (2012) 599-603.

[78] Y. Shiraishi, S. Kanazawa, Y. Kofuji, H. Sakamoto, S. Ichikawa, S. Tanaka, T. Hirai, Angewandte Chemie International Edition 53 (2014) 13454-13459.

[79]J.L. Yuan, X. Liu, Y.H. Tang, Y.X. Zeng, L.L. Wang, S.Q. Zhang, T. Cai, Y.T. Liu, S.L. Luo, Y. Pei, C.B. Liu, Applied Catalysis B-Environmental 237 (2018) 24-31.

[80] G. Zuo, S. Liu, L. Wang, H. Song, P. Zong, W. Hou, B. Li, Z. Guo, X. Meng, Y. Du, T. Wang, V.A.L. Roy, Catalysis Communications 123 (2019) 69-72.

[81] Y. Kofuji, S. Ohkita, Y. Shiraishi, H. Sakamoto, S. Tanaka, S. Ichikawa, T. Hirai, ACS Catalysis 6 (2016) 7021-7029.

[82] Z. Zhu, H. Pan, M. Murugananthan, J. Gong, Y. Zhang, Applied Catalysis B-Environmental 232 (2018) 19-25.

[83] S. Zhao, X. Zhao, H. Zhang, J. Li, Y. Zhu, Nano Energy 35 (2017) 405-414.

[84] Y. Yang, Z. Zeng, G. Zeng, D. Huang, R. Xiao, C. Zhang, C. Zhou, W. Xiong, W. Wang, M. Cheng, W. Xue, H. Guo, X. Tang, D. He, Applied Catalysis B: Environmental 258 (2019) 117956.

[85] Z. Wei, M. Liu, Z. Zhang, W. Yao, H. Tan, Y. Zhu, Energy & Environmental Science 11 (2018) 2581-2589.

[86] G.-h. Moon, M. Fujitsuka, S. Kim, T. Majima, X. Wang, W. Choi, ACS Catalysis 7 (2017) 2886-2895.

[87] S. Zhao, T. Guo, X. Li, T. Xu, B. Yang, X. Zhao, Applied Catalysis B-Environmental 224 (2018) 725-732.

[88] X. Li, J. Zhang, F. Zhou, H. Zhang, J. Bai, Y. Wang, H. Wang, Chinese Journal of Catalysis 39 (2018) 1090-1098.

[89] S. Li, G. Dong, R. Hailili, L. Yang, Y. Li, F. Wang, Y. Zeng, C. Wang, Applied Catalysis B-Environmental 190 (2016) 26-35.

[90] J. Goclon, K. Winkler, Applied Surface Science 462 (2018) 134-141.

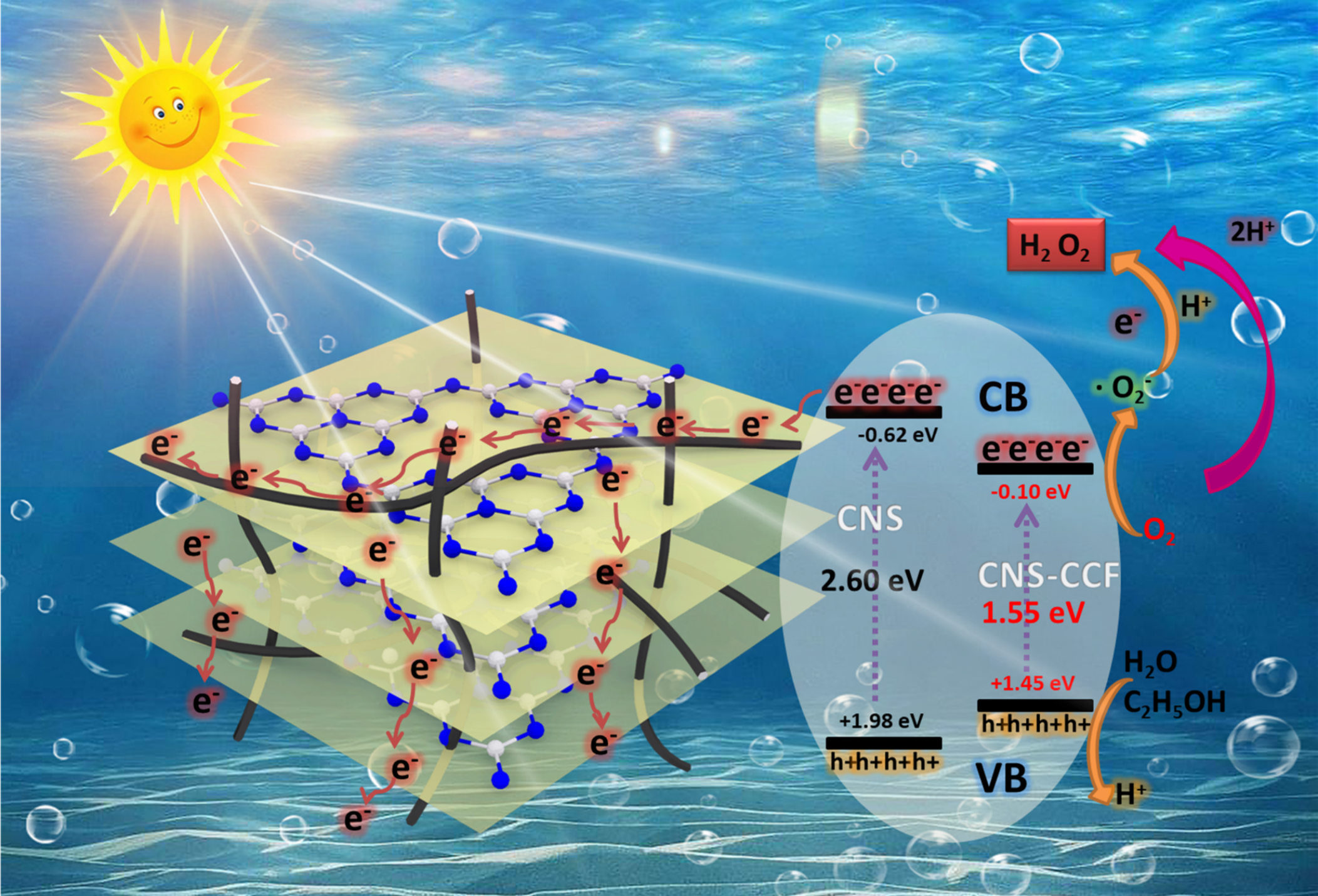
e⁻e⁻e⁻e⁻
CB
-0.62 eV
e⁻e⁻e⁻e⁻
-0.10 eV
CNS
2.60 eV
CNS-CCF
1.55 eV
+1.45 eV
+1.98 eV
h+h+h+h+
h+h+h+h+
VB
H₂O₂
2H⁺
e⁻
H⁺
·O₂⁻
O₂
H₂O
C₂H₅OH
H⁺